remote sensing

MDPI

Article

Deep Tectonic Environment Analysis of the Lingshan Conjugate Earthquake within the Qinzhou Fold Belt, South China: Insights Derived from 3D Resistivity Structure Model

Chunheng Yan [1,†], Bin Zhou [1,†], Yan Zhan [2,*], Xiangyu Sun [2], Sha Li [1], Lei Li [1] and Peilan Guo [1]

[1] Earthquake Agency of Guangxi Zhuang Autonomous Region, Nanning 530022, China; yan0112@163.com (C.Y.); dztzb@163.com (B.Z.); lisha4340@163.com (S.L.); lilei1941273117@163.com (L.L.); guopeilan550531839@163.com (P.G.)
[2] State Key Laboratory of Earthquake Dynamics, Institute of Geology, China Earthquake Administration, Beijing 100029, China; sunxiangyu@ies.ac.cn
* Correspondence: zhanyan@ies.ac.cn
† These authors contributed equally to this work.

Abstract: The Qinzhou fold belt, situated at the contact zone between the Yangtze and Cathaysia blocks in South China, was affected by the 1936 Lingshan M6¾ earthquake and the 1958 Lingshan M5¾ earthquake, both of which occurred within the conjugate structure. Understanding the deep seismogenic setting and causal mechanism of the Lingshan conjugate earthquake is of great significance for assessing the seismic disaster risk in the region. In this study, we utilized 237 magnetotelluric datasets and employed three-dimensional electromagnetic inversion to characterize the deep-seated three-dimensional resistivity structure of the Qinzhou fold belt and the Lingshan seismic zone. The results reveal that: (1) The NE-trending faults within the Qinzhou fold belt and adjacent areas are classified as trans-crustal faults. The faults exhibit crust-mantle ductile shear zones in their deeper sections, which are essential in governing regional tectonic deformation and seismic activity; (2) The electrical structure of the Qinzhou fold belt is in line with the tectonic characteristics of a composite orogenic belt, having experienced several phases of tectonic modification. The southeastern region is being influenced by mantle-derived magmatic activities originating from the Leiqiong area over a significant distance; (3) In the Lingshan seismic zone, the NE-trending Fangcheng-Lingshan fault is a trans-crustal fault and the NW-trending Zhaixu fault is an intra-crustal fault. The electrical structure pattern "two low, one high" in the zone has a significant impact on the deep tectonic framework of the area and influences the deformation behavior of shallow faults; and (4) The seismogenic structure of the 1936 Lingshan M6¾ earthquake was the Fangcheng-Lingshan fault. The earthquake's genesis was influenced by the coupling effect of tectonic stress and deep thermal dynamics. The seismogenic structure of the 1958 Lingshan M5¾ earthquake was the Zhaixu fault. The earthquake's genesis was influenced by tectonic stress and static stress triggering from the 1936 Lingshan M6¾ earthquake. The conjugate rupture mode in the Lingshan seismic zone is influenced by various factors, including differences in physical properties, rheology of deep materials, and the scale and depth of fault development.

Keywords: Qinzhou fold belt in South China; Lingshan conjugate earthquake; magnetotelluric imaging; 3D inversion

Citation: Yan, C.; Zhou, B.; Zhan, Y.; Sun, X.; Li, S.; Li, L.; Guo, P. Deep Tectonic Environment Analysis of the Lingshan Conjugate Earthquake within the Qinzhou Fold Belt, South China: Insights Derived from 3D Resistivity Structure Model. *Remote Sens.* **2024**, *16*, 3740. https://doi.org/10.3390/rs16193740

Academic Editor: Gabriel Vasile

Received: 15 August 2024
Revised: 29 September 2024
Accepted: 2 October 2024
Published: 9 October 2024

1. Introduction

Conjugate faults are a frequently observed fracture distribution pattern in the continental crust. Many earthquakes have been linked to concurrent fault movements, such as the Iceland M_W6.4 and M_W6.1 earthquakes in 1998 [1], the Ludian M_W6.1 earthquake in Yunnan, China in 2014 [2], and the central Italy M_W6.5 earthquake in 2016 [3]. Assessing seismic hazard risks in areas with conjugate faults can be quite challenging. This is due

to the widespread distribution of these faults, the complex nature of the earthquakes they produce, their frequent occurrences, and the overlapping impacts they can have on disasters. Through decades of exploration, geologists and seismologists have made significant progress in understanding the structure [4,5], mechanisms of conjugate ruptures [6–8], seismogenic structures [9,10], rupture processes [11,12], and stress triggering effects of conjugate faults [13,14]. However, research on the relationship between conjugate seismic ruptures and the deep tectonic environment remains limited [15]. Seismic ruptures in modern times often occur in areas with established tectonic environments, and many earthquake ruptures follow the path of pre-existing faults that extend deep into the Earth. Conjugate faults, which have developed over a significant period of geological time, exhibit a wide range of sizes, depths, and characteristics. As a result, they display variations in fault activity, strength against impedance, and degree of locking when subjected to current tectonic stress and deep dynamic processes [16]. Therefore, exploring the dynamics of how the deep tectonic environment in conjugate seismic zones controls or constrains the rupture behavior of shallow faults, and deepening the understanding of the mechanisms of conjugate seismic ruptures, are crucial for scientifically evaluating and mitigating seismic hazards in complex conjugate tectonic regions.

The South China Block (SCB) is a major continental block in East Asia. It is positioned opposite the North China Block (NCB) and is divided from it by the Qinling-Dabie orogenic belt (QDOB) in the north. It is connected to the Songpan-Ganzi Block (SGB) and shares a border with the Indochina Block (IB) in the southwest. Additionally, it is adjacent to the South China Sea Block (SCSB) in the southeast (Figure 1a). Although surrounded by some active fault zones such as the Longmenshan and Red River fault zones, the SCB experienced minimal large-scale tectonic deformation during the Cenozoic era [17]. This is in line with the current low rates of crustal deformation [18]. Overall, since the neotectonic period, the SCB has been relatively stable with low levels of seismic activity [19]. However, the Qinzhou fold belt (QZFB), located at the southwestern end of the tectonic junction zone between the Yangtze Block (YB) and the Cathaysia Block (CB) (Qinzhou Bay-Hangzhou Bay Tectonic Junction Zone, QHJB), is significantly different. This area features two sets of faults, NE-trending and NW-trending, forming an "X"-shaped conjugate fault framework. In the last 400 years, the QZFB and its surrounding areas have witnessed a total of 14 earthquakes with a magnitude of 5 or higher. Among these, there have been 5 earthquakes with a magnitude of 6 or higher, which indicates that the region is highly prone to seismic activity in the SCB (Figure 1b). Notably, the M6¾ earthquake that struck Pingshan Town, Lingshan County, Guangxi, on 1 April 1936, is the largest recorded inland earthquake in SCB, affecting an area of 500,000 km^2, causing the collapse of over 5800 houses and 101 deaths, with an elliptical distribution of seismic intensity in the SW-NE direction [20]. On 25 September 1958, a significant earthquake struck Shitang Town, Lingshan County. This earthquake, measuring M5¾ on the Richter scale, occurred approximately 6 km northwest of the epicenter of the 1936 earthquake. The seismic intensity lines from this event had an elliptical distribution, stretching in the NW-SE direction [21]. The epicenters of both earthquakes are located at the conjugate intersection of the NE-trending Fangcheng-Lingshan fault (FLf) and the NW-trending Zaixu fault (ZXf) (Figure 1b). The FLf is a large regional fault zone with obvious dextral strike-slip properties and seismicity-segmented characteristics. From southwest to northeast, it comprises the Fangcheng, Pingji, Lingshan, and Shinan segments [22]. Out of all the segments, the Lingshan segment has been the most active and has shown activity since the Late Pleistocene. Recent geological and geomorphological survey features have confirmed that the fault in the eastern branch of this segment is the fault responsible for the 1936 Lingshan M6¾ earthquake [23,24]. The ZXf develops along the boundary between granite mountains and erosional basins or linear valleys, and rivers along its path display sinistral displacement, indicating recent and active fault movements. The differing shapes of the intensity lines of the two earthquakes suggest differences in their seismogenic structures and rupture mechanisms. Zhou et al. [25] presented a resistivity structure model from a broadband magnetotelluric (MT) survey profile crossing the QZFB

(blue dots in Figure 1b represent part of the profile), providing characteristics of the deep electrical structure and deep extension of major faults along the profile. Currently, the understanding of the deep structural characteristics and the deep environment of the conjugate fault system in the Qinzhou fold belt is still incomplete, and the seismogenic structure of the 1958 M5¾ earthquake and the relationship between the deep structures of the two earthquakes have not been reported.

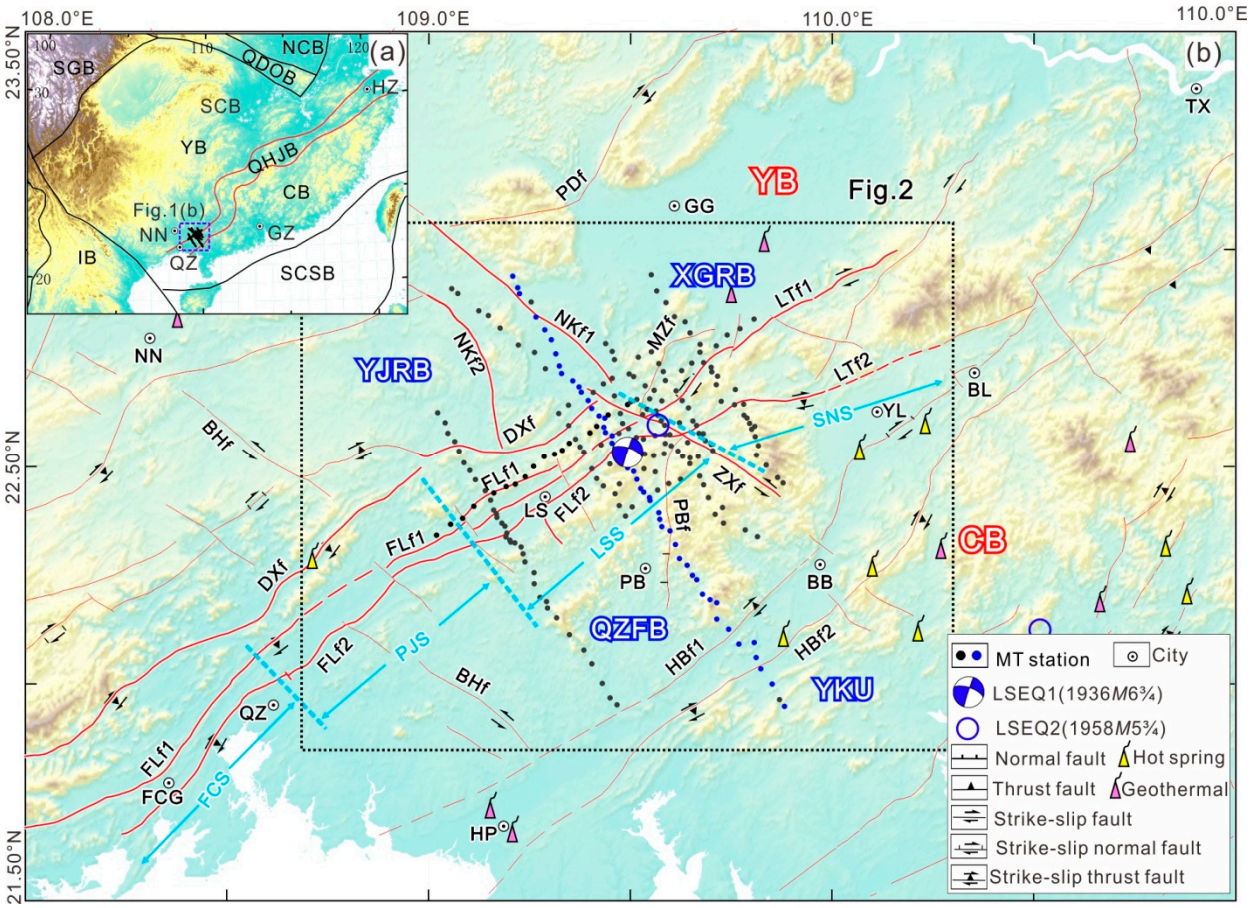

Figure 1. Geotectonic diagrams of SCB and its neighboring zones and topography, fault, and magnetotelluric (MT) points distribution maps in the study area. (**a**) Geotectonic diagrams of SCB and its adjacent zones (modified from [26,27]). North China Block (NCB), South China Block (SCB), Yangtze Block (YB), Cathaysian Block (CB), Songpan-Ganzi Block (SGB), Indochina Block (IB), South China Sea Block (SCSB), Qinling-Dabie Orogen belt (QDOB) [26]; Qinzhou Bay-Hangzhou Bay Tectonic Junction Zone (QHTJZ [27]). (**b**) Topography map of Qinzhou Fold Belt (QZFB), and fault structure and MT line distribution maps in the study area. Youjiang Rift Basin (YJRB), Xianggui Rift Basin (XGRB), Yunkai Uplift (YKU). Western Fangcheng-Lingshan fault (FLf1), Eastern Fangcheng-Lingshan fault (FLf2), Western Lingshan-Tengxian fault (LTf1), Eastern Lingshan-Tengxian fault (LTf2), Northern Nandan-Kunlunguan fault (NKf1), Southern Nandan-Kunlunguan fault (NKf2), Western Hepu-Beiliu fault (HBf1), Eastern Hepu-Beiliu fault (HBf2), Zhaixu fault (ZXf), Guilin-Nanning fault (GNf), Pingxiang-Dali fault (PDf), Baise-Hepu fault (BHf), Dongzhong-Xiaodong fault (DXf), Pubei fault (PBf), Muzi fault (MZf). Segmenting of FLf, Fangheng segment (FCS), Pingji segment (PJS), Lingshan segment (LSS), and Shinan segment (SNS). Nanning (NN), Qinzhou (QZ), Fangchenggang (FCG), Guigang (GG), Tengxian (TX), Yulin (YL), Beiliu (BL), Lingshan (LS), Pubei (PB), Bobai (BB), Hepu (HP).

Over the past few years, the growing advancement of 3D MT inversion technology and the increasing computational capabilities have led to the widespread utilization of 3D MT arrays [28–30]. These arrays have proven to be valuable in detecting intricate seismogenic

structures and deep seismogenic environments in areas prone to strong earthquakes, such as Wenchuan, Lushan, and Jiuzhaigou [31–35]. The electromagnetic detection with dense measuring points has also revealed that differences in the activity of various segments of fault zones are closely related to the characteristics of deep medium development [36–40]. The article presents findings from the magnetotelluric array detection conducted in the Qinzhou fault fold belt and surrounding regions. The integration of seismic geology, GPS data, terrestrial heat flow measurements, and static stress triggering provides insights into the deep electrical structure of the fault system and the block within the Qinzhou fault fold belt. Additionally, this approach facilitates an exploration of the deep tectonic setting and seismogenic mode associated with the Lingshan conjugate earthquake.

2. Regional Geological Structure and MT Profile

The Qinzhou fold belt (QZFB) is located at the southwestern end of the contact zone between the Yangtze Block (YB) and the Cathaysia Block (CB) in the South China Block (Figure 1b). This region experienced various stages of tectonic deformation, amalgamation, superposition, and modification, recording significant processes of crust-mantle material migration and interaction [41,42]. Divided by the Eastern Fangcheng-Lingshan fault (FLf2), Eastern Lingshan-Tengxian fault (LTf2), and Western Hepu-Beiliu fault (HBf1), the QZFB comprises three secondary tectonic units: Lingshan Fold Belt (LSFB), Liuwandashan Uplift (LWDSU), and Bobai Fold Basin (BBFB) (Figures 1b and 2). The LSFB primarily comprises acidic magmatic rocks and strata dating back to the Paleozoic, Mesozoic, and Cenozoic eras [43,44]. The LWDSU is a region characterized by Hercynian-Indosinian granites that are the dominant geological feature. The BBFB is an ancient composite subduction accretion complex and collision zone [45,46]. The northwestern area of the QZFB has a relatively uniform pre-Nanhua basement, but it was reactivated by multiple orogenic events from the Early Paleozoic to Mesozoic, making it a disrupted cratonic unit [26]. The region is defined by the fault known as the Nandan-Kunlun Pass fault (NKf), which separates it into two basins: the Youjiang Rift Basin (YJRB) and Xianggui Rift Basin (XGRB) in the northwest. Figure 2 displays the secondary geological units of the YJRB's Shiwandashan Fault Depression (SWDSFD) and the XGRB's Dayaoshan Fault Depression (DYSFD) (Figure 1b). The SWDSFD is a Late Triassic to Middle Jurassic foreland basin primarily composed of fluvial sand-gravel rock series, with a central sedimentary thickness exceeding ten thousand meters [47–49]. The DYSFD is a subsidence zone located along a continental margin. It is composed of folded basement rocks from before the Ordovician period and a sedimentary cover made up of carbonate deposits from the Late Paleozoic era. On top of these layers are deposits from the Cretaceous period [50]. On the southeastern side of the QZFB, the Yunkai Uplift (YKU) is the oldest area of mixed crystalline basement and greenschist facies metamorphic folded basement in the South China Block. Extensive development of medium-acid intrusive rock bodies has occurred during various periods as a result of intense tectonic-magmatic activity [51–53].

The study area is characterized by two sets of deep-seated fault zones that trend in a northeast and northwest direction, creating an eye-catching "X"-shaped conjugate fault system (Figure 1b). The fault zones that trend towards the northeast are quite significant, with extended periods of activity. These faults are intricate and exhibit a dextral strike-slip behavior since the neotectonic period. These include the Pingxiang-Dali fault (PDf), Dongzhong-Xiaodong fault (DXf), Fangcheng-Lingshan fault (FLf), Lingshan-Tengxian fault (LTf), and Hepu-Beiliu fault (HBf). It should be noted that Zhou et al. [22], based on surface seismic geological survey data, consider the LTf as part of the FLf, referring to it as the Shinan segment of the FLf. However, considering the significant differences in deep extension direction, geometric structure, and deep environment revealed in this study, the LTf is named separately here. Fault zones with a northwest orientation are consistently present in the northwestern portion of the study area and occasionally appear in the southeastern part. They primarily formed during the tectonic disintegration of the Late Paleozoic carbonate platform and have displayed sinistral strike-slip activity since the

neotectonic period, including the Nandan-Kunlun Pass fault (NKf), Zaixu fault (ZXf), and Baise-Hepu fault (BHf) [41,43,47,49].

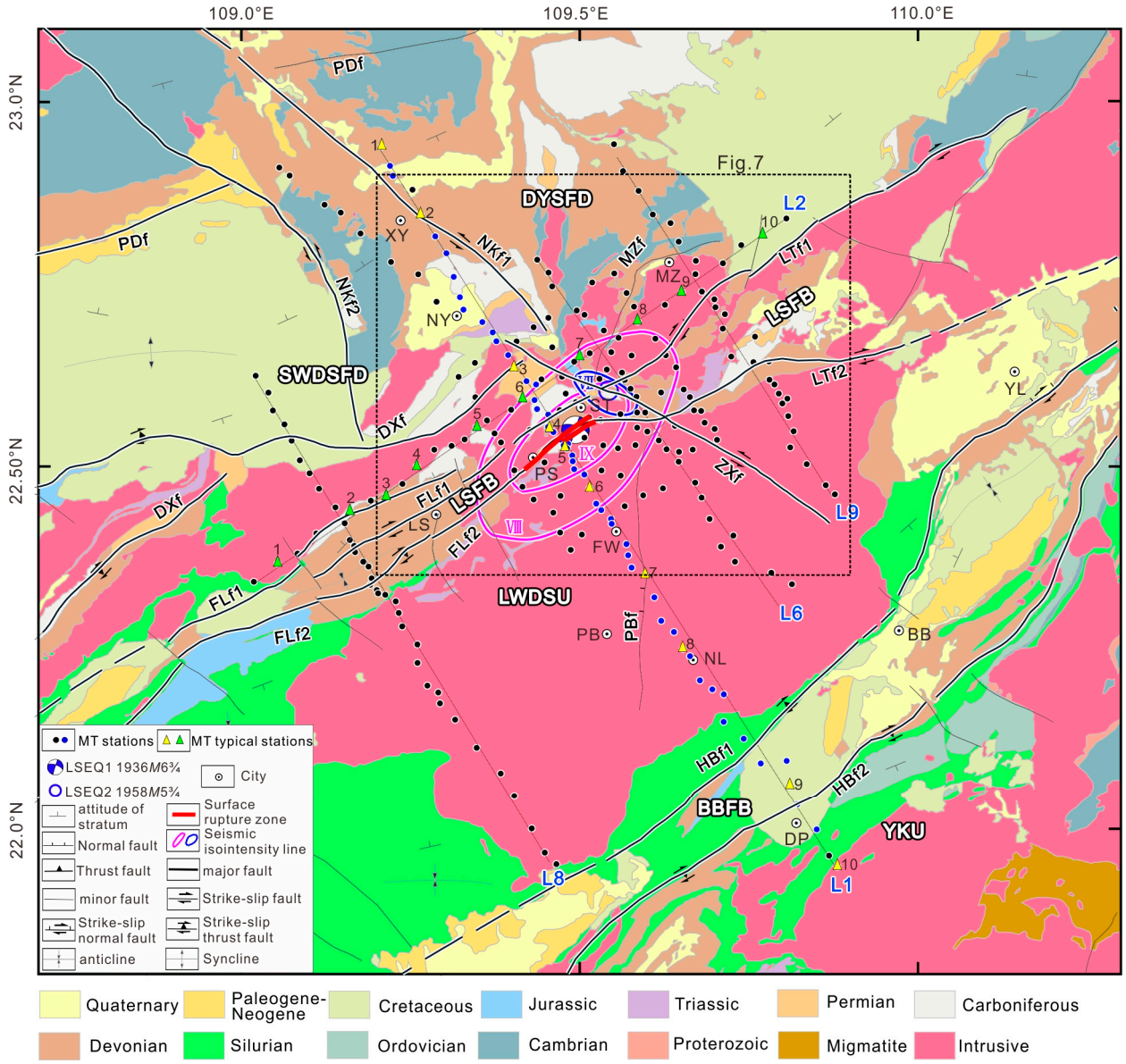

Figure 2. Geological structure and MT point distribution of the Lingshan earthquake zone and its adjacent areas. Dayaoshan Fault Depression (DYSFD), Shiwandashan Fault Depression (SWDSFD), Lingshan Fold Belt (LSFB), Liuwandashan Uplift (LWDSU), Bobai fold Basin (BBFB). Xiaoyi (XY), Nayang (NY), Nalin (NL), Fuwang (FW), Muzi (MZ), Dongping (DP), Pingshan (PS), Shitang (ST). The names of faults are consistent with those in Figure 1.

An MT detection network was constructed based on the distribution of conjugate structures and segmental features of NE-trending fault activity in the QZFB and nearby locations. This network comprises four NW-SE trending main profiles (L8, L1, L6, L9), one SW-NE trending main profile (L2), and a 3D MT array covering the Lingshan seismic zone, resulting in data from 237 measurement points. The L8 and L1 profiles cross the Lingshan segment of the FLf, the L6 profile crosses the junction of the FLf Lingshan segment and the LTf, and the L9 profile traverses the LTf. The L1 profile traverses the macro-epicenter region of the 1936 Lingshan earthquake. It begins around 10 km northeast of Xiaoyi in the northwest and extends through Nayang, Pingshan, Fuwang, and Nalin, concluding

approximately 8 km south of Dongping in the southeast. The profile spans a distance of approximately 130 km and includes 56 measurement points. The L8 profile is about 88 km long with 35 measurement points, the L6 profile is about 63 km long with 29 measurement points, the L9 profile is about 63 km long with 28 measurement points, and the L2 profile traverses the LSFB, with a length of about 98 km (Figures 1 and 2).

3. Data Analysis

3.1. Data Collection and Processing

In 2017, a total of 200 measurements of magnetic susceptibility (MT) data were gathered in the Lingshan seismic zone. In 2019, an extra 37 data points were included in the northwest and southeast parts of the research area. The MT data for both periods were collected using the MTU-5A system from Phoenix Geophysics, Canada. Each site recorded five components of MT data, including the electric field components in the north-south and east-west directions and the magnetic field components in the north-south, east-west, and vertical directions. As a result of the intricate electromagnetic surroundings and substantial electromagnetic interference along the profile, the duration of data collection at each location surpassed 40 h, with some sites taking up to 50 h. In addition, a remote reference station was set up near Xiangzhou in the northeast of the study area to apply remote reference [25] and robust processing techniques [54,55], which improved data quality and enhanced the continuity of the apparent resistivity and phase curves.

Figure 3a displays the apparent resistivity curves for 10 representative measurement points along profile L1, situated within the DYSFD, LSFB, LWDSU, BBFB, and YKU units. The apparent resistivity curves within these five structural components exhibit clear distinctions. The apparent resistivity values for points 1 and 2 exceed tens of thousands Ωm in the high-frequency band above tens of hertz, dropping sharply to tens Ωm below this frequency, indicating a two-layer (high and low) resistivity structure in DYSFD. Measurement points 3 and 4 within LSFB show a gradual increase in apparent resistivity from hundreds to thousands Ωm with increasing periods, indicating a high-resistivity structure. However, point 5, situated in the eastern and western branches of FLf, has consistently lower apparent resistivity values, indicating the presence of a noticeable low-resistivity anomaly in FLf. The apparent resistivity curves of points 6, 7, and 8 in LWDSU and point 10 in YKU show an increase from nearly 100 Ωm in the high-frequency band to thousands of Ωm in the low-frequency band, presenting a two-layer (high and low) resistivity structure. The measured resistivity values for point 9 within BBFB are consistently low across all frequency bands, suggesting the presence of a structure with low electrical resistance in this particular area.

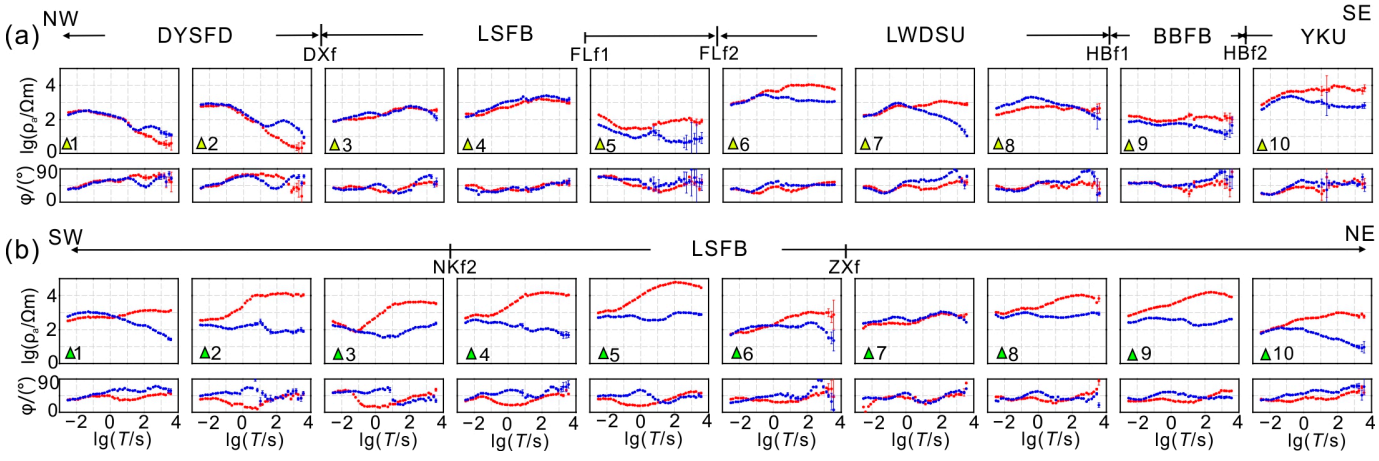

Figure 3. Apparent resistivity and phase curves for typical MT sites on profile L1 (**a**) and L2 (**b**) (see Figure 2 for the locations). Red points denote data in the XY direction, and blue points denote data in the YX direction. The names of construction units and faults are consistent with those in Figure 2.

Here are the apparent resistivity curves for 10 measurement points across LSFB on profile L2 (Figure 3b). The apparent resistivity values for all points show a general trend of being high across all frequency bands. However, there are two specific areas where the high-frequency apparent resistivity values are slightly lower compared to the measurement points on the surrounding sides. These areas are near the southeastern extension of NKf2 (points 3 and 4) and near ZXf (points 6 and 7). This indicates that while the deep structure of LSFB is generally high-resistivity, NW-trending faults may influence the shallow structure of LSFB, causing variations in the electrical properties near the fault zones.

3.2. Analysis of Dimensionality and Electrical Differences

Understanding phase tensor decomposition is essential for effectively analyzing electromagnetic data. The two-dimensional (2D) phase tensor skew (β) can be used to identify the dimensional characteristics of underground structures [56,57]. Considering measurement errors, a $|\beta|$ value greater than 5 is indicative of strong 3D characteristics in deep structures [58,59].

The distribution of 2D phase tensor skew is depicted in Figure 4a–c for three different periods. For periods above 0.1 s in the high-frequency band, $|\beta|$ is generally less than 5, indicating weak 3D characteristics in the shallow structure. Between 0.1 s and 14 s, certain measurement points in the Lingshan seismic zone and its northern area display $|\beta|$ values that surpass 5. As the period continues to increase, the majority of $|\beta|$ values consistently exceed 5, suggesting significant 3D characteristics in the deep structure of the study area. The Lingshan seismic zone, in particular, shows especially strong 3D characteristics, reflecting the complex development of NW-trending and NE-trending faults in the deep structure.

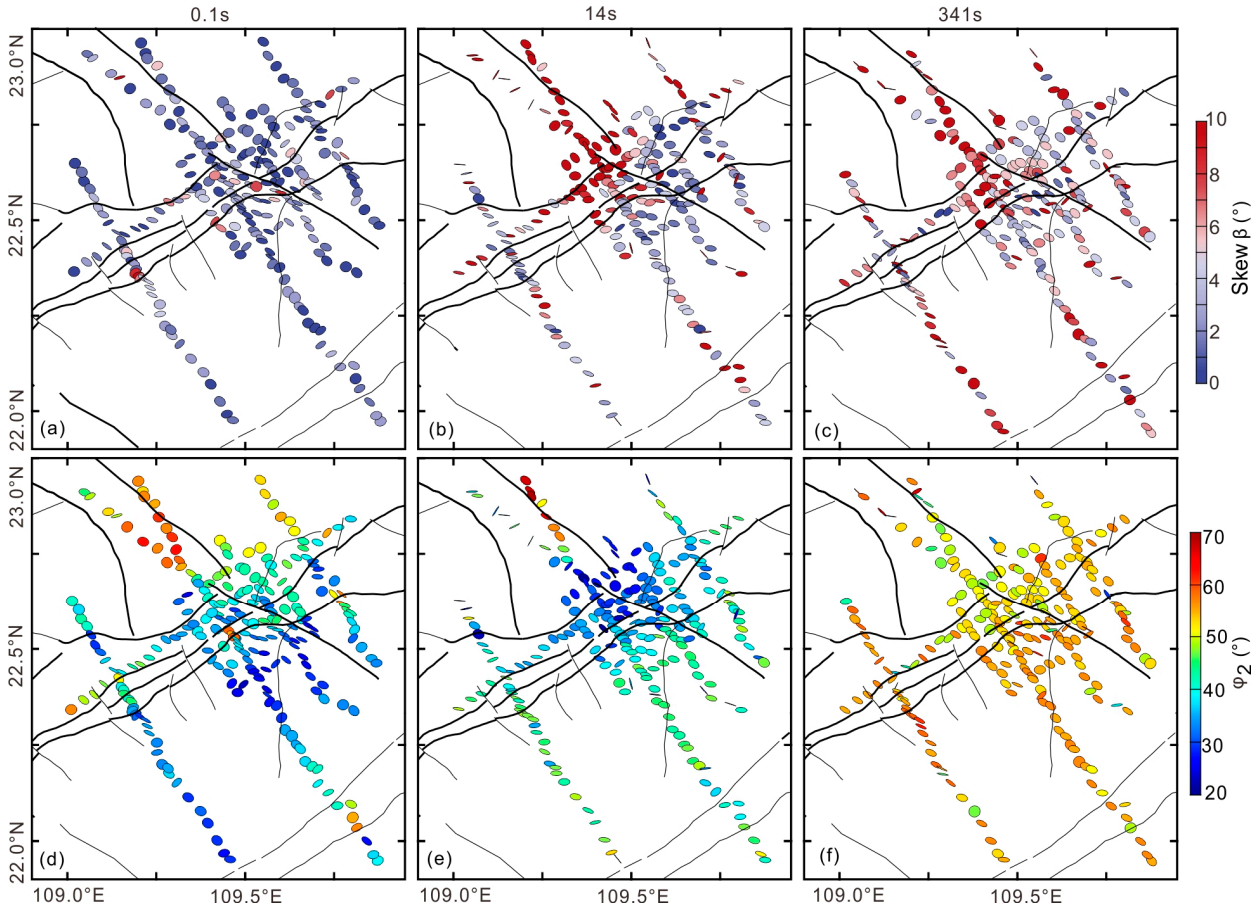

Figure 4. (**a**–**c**) Phase tensor ellipses filled with absolute value of skew angle β for periods of 0.1 s, 14 s, 341 s. (**d**–**f**) Phase tensor ellipses filled with phase tensor invariant for periods of 0.1 s, 14 s, 341 s.

Figure 4d–f present the phase invariant φ2 [60] for three different periods. For periods above 0.1 s in the high-frequency band, φ2 shows high-phase values on the northwest side of DXf and LTf1 and low-phase values on the northeast side. Between 0.1 s to 14 s, the northwest side consistently shows high-phase values, while the northeast side exhibits low-phase values. As the period increases further, φ2 tends to become more uniform with medium to low-phase values. DXf and LTf1 represent separate areas with differing electrical properties. The low-resistivity characteristics are typically observed on the northwest side, while the southeast side is associated with high-resistivity structures.

4. 3D Inversion

Due to the intricate fault system and significant skew values in the 2D phase tensor in the Lingshan study area, deep electrical structure images were obtained by conducting a 3D inversion using ModEM software [28]. Before inversion, data from all measurement points were interpolated uniformly across frequency points, resulting in 44 effective interpolated frequency points ranging from 0.003125 to 7300 s. The inversion process utilized selected data for apparent resistivity and impedance phase. Threshold errors were then established at 10% and 2.84°, respectively.

The horizontal grid division of the 3D inversion model consisted of the core area that covered all the measurement points and boundary grid divisions. The central region of the Lingshan seismic zone was divided into a grid with a spacing of 1 km × 1 km, ensuring uniform measurement point distribution in the core area. The divided grid was 116 (north-south) × 94 (east-west), and 10 additional expansion grids were arranged in each direction, totaling 136 × 114 grids. Vertical grid division was conducted without terrain considerations. The initial grid thickness was set at 20 m and gradually increased in segments at varying growth factors. Within the first 0.5 km, the growth factor was 1.2. From 0.5 to 1 km, the growth factor was 1.1. From 1 to 15 km, the growth factor was 1.05. From 15 to 150 km, the growth factor was 1.1. Finally, from 150 to 500 km, the growth factor was 1.2. This layering approach resulted in a total of 87 layers (Figure S1). A homogeneous half-space model of 500 Ωm was used as the initial model, and the regularization factors were updated automatically. The initial regularization factor was set at 5000, and when the inversion stopped converging, the regularization factor was adjusted to one-tenth of the original value to continue the inversion process. After 83 iterations, the model was able to achieve a root mean square (RMS) error of 1.46. Figure 5 shows the fitting residual distribution of apparent resistivity and impedance phase in the north-south and east-west directions, indicating good fitting quality. Figure S2 presents the fitting curves of the 3D inversion response for all measurement points in comparison to the observed apparent resistivity and impedance phase data. The test results from forward modeling (Figures S3–S5) validate the reliability of the resistivity model and the primary anomaly bodies within the crust (R1, C3, etc., as illustrated in Figures 6 and 7).

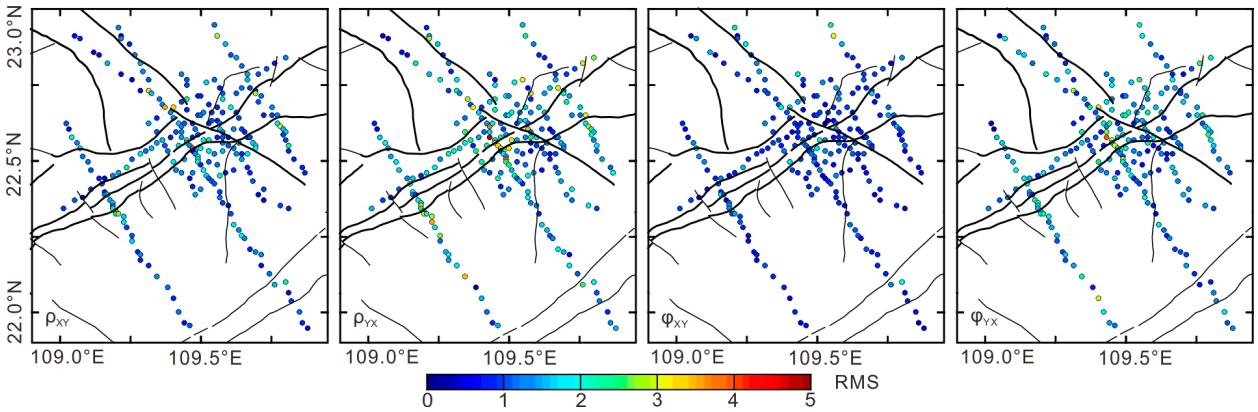

Figure 5. RMS Misfit distribution of the 3D inversion.

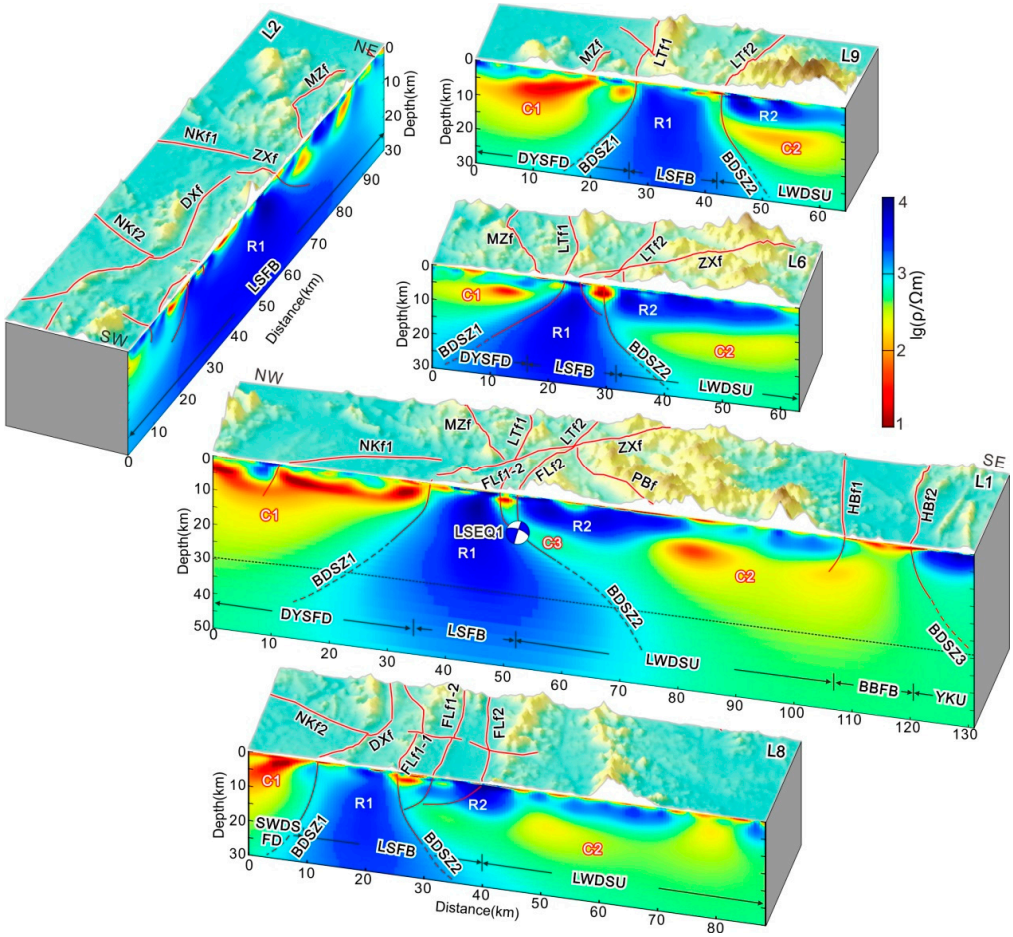

Figure 6. Five cross sections extracted from the 3D Model. (See Figure 2 for the locations of cross sections). The names of construction units and faults are consistent with those in Figures 1 and 2.

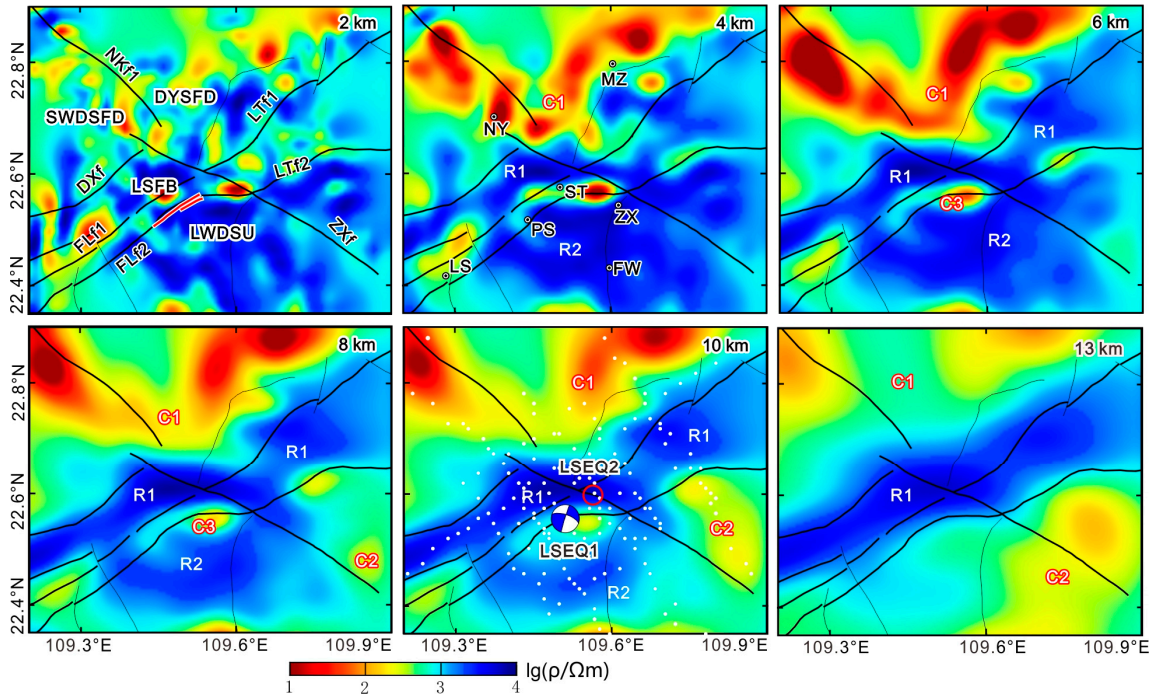

Figure 7. Electrical structure slices of the Lingshan earthquake zone (see Figure 2 for the locations). Black lines denote faults, red lines denote coseismic surface rupture zone.

5. Results and Discussion

5.1. Lateral Distribution Characteristics of the Deep Electrical Structure in the Qinzhou Fold Belt and Adjacent Areas

Figure 6 presents the 3D resistivity structure model across several profiles. The L8, L1, L6, and L9 profiles run from northwest to southeast, while the L2 profile runs from southwest to northeast. The L1 profile specifically shows the depth of the Moho, ranging from 29.3 km in the northwest to 28.0 km in the southeast [61]. The interpretation of the fault systems and the deep structural characteristics in tectonic elements were based on surface geology and electrical structural characteristics.

The electrical structures along the four NW-SE profiles reveal that both DXf and LTf1 are high and low-resistivity boundary zones dipping (Figure 6 BDSZ1) NW and extending beyond the Moho, suggesting large-scale ductile shear zones at depth. This information provides support for geological surveys and gravity exploration, which have identified this line as a significant boundary in the tectonic lithofacies of the SCB [41]. FLf and LTf2 dip southeast and display low-resistivity bands buried within high-resistivity bodies R1 and R2 in the upper crust, transitioning to high and low-resistivity boundary zones in the lower crust-upper mantle, potentially indicating the deep extension of surface brittle-ductile shear zones [62] (Figure 6 BDSZ2). Based on profile L1, it is evident that both HBf1 and HBf2 exhibit properties that resemble resistivity boundary zones in terms of their electrical structure. More specifically, there is a dip in the NW direction for HBf1 that goes beyond a depth of 5 km. On the other hand, HBf2 has a dip in the SE direction that also extends to a significant depth. Previous MT surveys [25,63] and geological investigations [41] suggest that HBf2 represents a ductile shear zone in the lower crust-upper mantle, corresponding to the surface-exposed brittle-ductile shear deformation zone (Figure 6 BDSZ3). Profile L2 reveals that ZXf is a high and low-resistivity boundary zone dipping NE, extending approximately 10 km. Three NW-trending branch faults are developed within the LSFB on the southeast side of NKf2 (Figure 2). Two sections stretch out for a distance of 2–3 km, while the third section slopes towards the southwest and covers a length of around 10 km. This third section may represent the continuation of NKf2 towards the deep southeast. To summarize, the faults in the study area run in a northeast direction and span across the Earth's crust. These faults have shear zones that extend into the mantle, and they play a crucial role in controlling regional tectonic deformation and seismic activity. In contrast, the NW-trending faults are developed within the upper crust, are smaller in scale, and play a subordinate role in regional tectonic deformation and seismic activity.

Separated by the deep-seated faults DXf and LTf1 (Figure 6), the SWDSFD and DYSFD in the northwest part of the survey area display similar electrical structures. Within the range from the shallow surface to about the depth of 2 km, there was a high-resistivity layer, corresponding to the Devonian–Middle–Lower Triassic carbonate, siliceous, and clastic sedimentary strata widely exposed on the surface. Between 2–10 km, a low-resistivity layer (C1) with resistivity values of several tens Ωm exists, displaying a northwest-deep, southeast-shallow distribution, corresponding to the Late Paleozoic intracontinental rift basin's carbonate sedimentary strata. Structures with medium-low resistivity are commonly observed below C1, which may indicate the presence of shallowly metamorphosed turbidite clastic rocks from the Pre-Devonian era. The central part of the survey area, the QZFB, consists of LSFB, LWDSU, and BBFB. The four NW-trending profiles show that LSFB develops high-resistivity bodies (>1000 Ωm) in the upper crust, corresponding to Hercynian–Indosinian granite intrusions (Figures 2 and 6). In the lower crust–upper mantle top, it displays a narrow top-wide bottom high-resistivity body (R1) with resistivity values reaching tens of thousands Ωm, possibly indicating deep physical properties of deep-sea facies turbidite clastic rock sediments and granite intrusions from the final closure of the rift trough [64,65]. The deep electrical structure of LWDSU exhibits a noticeable level of stratification. There is a high-resistivity structure (R2) in the northwest that deepens and becomes shallower in the southeast. It is observed at a depth of approximately twelve kilometers and has a resistivity value exceeding one thousand Ωm. This value is consistent

with the resistivity of the Variscan–Indosinian granite, which is extensively exposed on the surface. Below this structure, the resistivity decreases to several tens Ωm (C2), possibly indicating deep-sea to semi-deep-sea turbidite sediments. BBFB displays low-resistivity structures of several tens Ωm above 3 km, corresponding to the red clastic rock sediments of the Meso-Cenozoic basin. Below 5 km, the resistivity increases to several hundred Ωm and then decreases to 100–300 Ωm at greater depths, similar to the resistivity values of C2 below LWDSU. In the southeastern region of the survey area, YKU observes the presence of high-resistivity bodies in the upper crust and secondary low-resistivity bodies in the middle–lower crust to the upper mantle top. These findings align with previous research findings [25,63,66]. Overall, the deep electrical structures of DYSFD and SWDSFD are well stratified, aligning with the quasi-cratonic tectonic attributes of localized destruction at the southeastern margin of the YB. The electrical structures of QZFB and YKU exhibit a combination of high and low resistivity characteristics, which align with the tectonic attributes of a composite orogenic belt experiencing multiple phases of tectonic modification [26].

5.2. Conjugate Seismic Structures and Medium Properties in the Lingshan Seismic Zone

To analyze the properties of FLf and ZXf in the Lingshan seismic zone, a total of six depth slices (Figure 7) and eleven profiles of the electrical structure were made available. These slices and profiles help to uncover the unique seismic structures and medium properties of the area. Profiles L1 and L5 transect the seismogenic structures of the 1936 M6¾ earthquake and near the macroseismic epicenter, and profile NE3 passes through the macroseismic epicenter of the 1958 M5¾ earthquake (Figure 8).

Based on Figure 7, it can be observed that seismic activity at depths below 2 km exhibits a pattern of alternating high and low resistivity distributions. These distributions are associated with surface faults of different orientations and sizes, as well as layers of sediment that have undergone multiple phases of deposition. Between 4–10 km, with DXf and LTf1 as boundaries, there is a stark contrast in electrical structures: the northwest side (DYSFD and SWDSFD) develops a distinct low-resistivity layer (C1), while the southeast side (LSFB) displays an overall high-resistivity structure (R1), connected to the intact high-resistivity structure (R2) below LWDSU. In the vicinity of the intersection of R1 and R2, there exists a body with low resistivity (C3) that is spread out along FLf2. This body extends to the surface and encompasses the area where the surface rupture occurred during the 1936 M6¾ earthquake, as well as the location of the macroseismic epicenter of the 1958 M5¾ earthquake. Below 10 km, the overall pattern is a "two low, one high" electrical structure, i.e., a continuous high-resistivity body (R1) along LSFB is flanked by relatively continuous low-resistivity bodies (C1, C2). Zhou et al. [25] suggest that the high-resistivity body R1 is possibly related to lithospheric delamination following the orogenic collision between the Yangtze and Cathaysia blocks. In contrast to the low-resistivity bodies C1 and C2 flanking it, the high-resistivity body R1 exhibits a harder lithology and higher viscosity. This characteristic has the potential to influence the deep tectonic framework and limit the deformation behavior of shallow faults within the seismic zone.

Figure 8 provides a comprehensive view of the extensive fault extension within the seismic zone. Based on the NW–SW profiles (Figure 8a), it can be observed that FLf's two branch faults in the Lingshan segment are found within low-resistivity bands within the high-resistivity body above 10 km. Around 10 km, the two branches converge, dipping southeast and extending into the low-resistivity layer (C2) below LWDSU. The 1936 M6¾ earthquake occurred at the convergence point of the two branch faults (profiles L1, L4, and L5). The two branches of LTf dip in opposite directions, extending as single faults in relatively complex environments: LTf1 develops along high and low-resistivity boundaries (profiles L6 and L9) or low-resistivity bands (profile L7); LTf2 develops within the high-resistivity body (profile L7) or along low-resistivity bands (profile L9). This suggests that while FLf and LTf may appear similar in terms of tectonic geomorphology on the surface, they exhibit distinct variations in deep extension direction, geometric structure, and environmental setting. These differences align with the findings of surface geological surveys,

which indicate segmented characteristics of seismicity along FLf and LTf at depth [22]. The NE-trending profiles (NE1–NE5) in Figure 8b reveal that ZXf is a steeply dipping fault developed in the upper crust, and dips vary in different segments. With FLf as the boundary, the northwest segment dips NE, while the southeast segment dips SW, with decreasing depth towards the southeast, disappearing into the Pubei granite body. Notably, the dip change of ZXf occurs between FLf1 and FLf2, near the macroseismic epicenter of the 1958 M5¾ earthquake. From the analysis of the intensity distribution direction, it can be deduced that the point where the two faults intersect is the location where the 1958 M5¾ earthquake originated. The seismogenic structure responsible for this earthquake is ZXf.

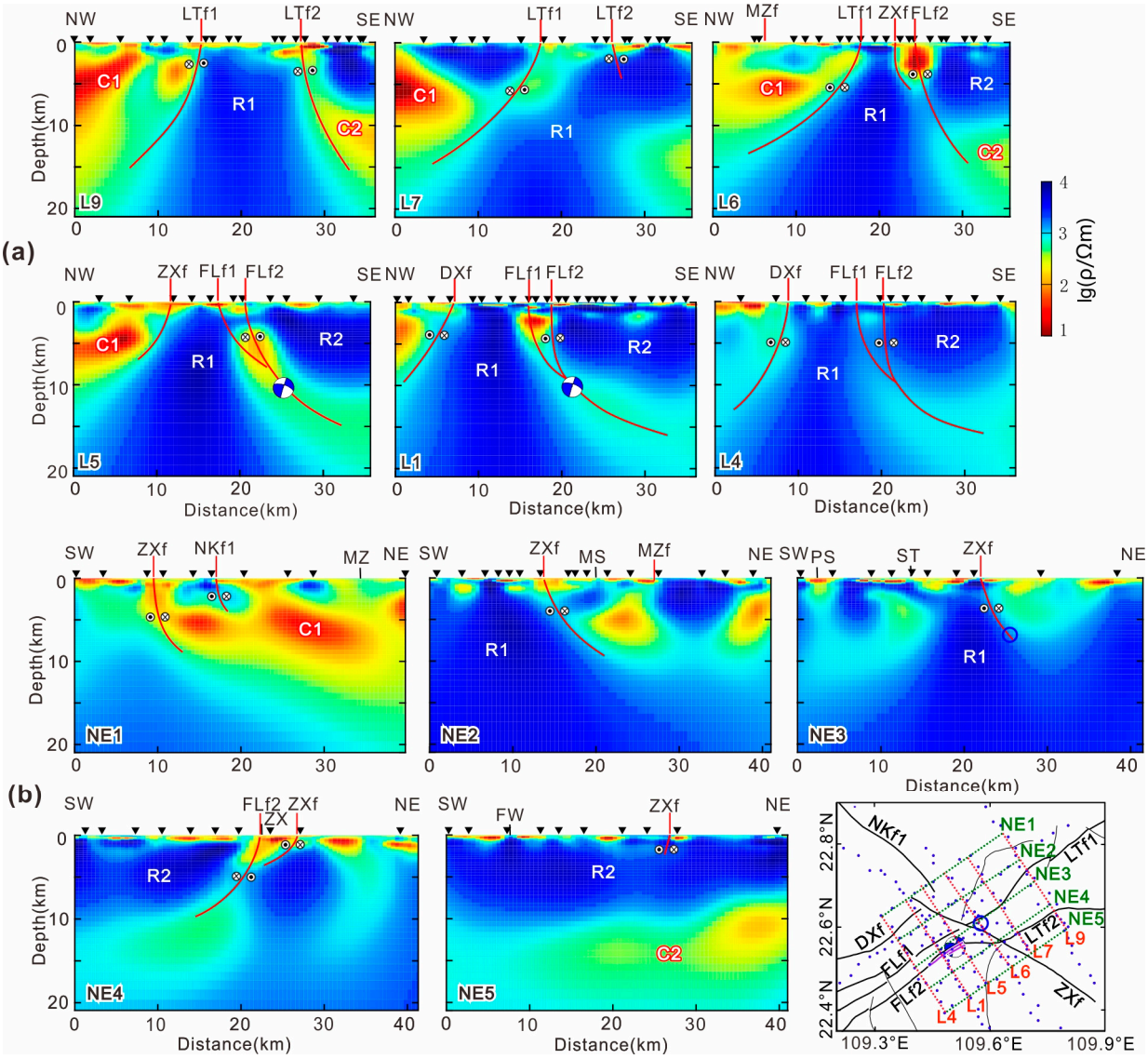

Figure 8. Electrical structure profiles of the Lingshan earthquake zone. "NE" represents a profile from southwest to northeast, and "L" represents a profile from northwest to southeast. The names of construction units and faults are consistent with those in Figures 1 and 2.

5.3. Seismogenic Patterns of Conjugate Earthquakes in the Lingshan Zone

The Lingshan seismic zone is made up of a fault system that forms an "X" shape, with faults trending in both the NE-trending and NW-trending directions. The conjugate area experienced the M6¾ earthquake in 1936 and the M5¾ earthquake in 1958, differing in magnitude by one unit and separated by an interval of 22 years, displaying asymmetric conjugate ruptures and time lag of rupture. Seismic ruptures in the present day occur

on top of the underlying tectonic conditions. The majority of ruptures can be attributed to the deep extension of pre-existing faults. Thus, the seismogenic patterns of conjugate earthquakes are closely related to the deep tectonic environment of the seismic zone. As previously mentioned, the physical properties and rheology of rocks below 10 km in the Lingshan seismic zone show an NE-trending zonal distribution, controlling the deep tectonic framework of the seismic area. The FLf fault extends on a larger scale across the crust, while the ZXf fault is smaller and contained within the crust. The differences in the physical characteristics, flow behavior, and extent and magnitude of fault formation are likely responsible for the seismic pattern of conjugate faults in the Lingshan seismic zone.

The GPS velocity fields and surface strain calculations in the Lingshan seismic zone and adjacent areas reveal a gradual decrease in velocity from the west to the east, with an average of 6.5 mm/a in the west to 4.3 mm/a in the east. This suggests horizontal compressive dynamics from northwest to southeast (Figure 9). The three GPS stations within the QZFB display lower movement rates compared to surrounding stations (Figure 9a), with nearly zero surface strain rate, corresponding to the projection of the gigantic high-resistivity body R1 to the surface in Figure 7. It appears that the decrease in crustal movement rate in this region is connected to the hindrance caused by the deep high-resistivity, rigid body. Since the late Cenozoic, the southeastern side of the study area has experienced multi-cycle volcanic eruptions in the Leiqiong area [67–69]. Geochemical and seismological studies indicate mantle material upwelling as the deep driving force [70–73]. In the Lingshan seismic zone, there are a variety of geological features to be found. These include Mesozoic intermediate-acid intrusive rocks (veins), Cenozoic basic volcanic rocks, numerous hot springs, and a low-resistivity layer (C2) that extends southeastwards in the deep. These suggest that this area is possibly influenced by the upwelling mantle-derived thermal material from the Leiqiong area [74,75]. Therefore, the Lingshan seismic zone is affected by both NWW–SEE horizontal compressions and deep thermal dynamics from the southeast. In the middle–lower crust of FLf2, a ductile shear zone with low rheological strength and viscosity adjusts the deformation of adjacent blocks through creep behavior and "slow earthquakes" under the coupling of regional tectonic stress and deep thermal dynamics. The high-resistivity bodies (R1) beneath the LSFB and (R2) in the upper crust of LWDSU, composed mainly of relatively "cold", "hard" intrusive rocks and flysch clastic rocks, display rigid body characteristics. These bodies experience strain due to regional tectonic stress and deep thermal dynamics, making them the main accumulators of tectonic stress. When the stress accumulates to the rock strength limit, it causes the relatively weaker FLf2 within the high-resistivity band to experience a dextral strike-slip rupture instability, leading to the occurrence of the Lingshan M6¾ earthquake (Figure 9b).

Various factors contribute to the process of stress accumulation and release in faults. These include regional tectonic stress, the physical properties of rock bodies, and the activity of adjacent faults. These interactions and seismic triggering play a significant role in shaping the overall behavior of faults [76,77]. Seismological investigations and focal mechanism studies show that the 1936 M6¾ Lingshan earthquake resulted from the dextral strike-slip rupture of FLf2. The coseismic elastic rebound would cause the upper crustal block northwest of FLf2 to displace NE-wards, particularly in the segment where FLf2 transitions from NE to NEE trending, facilitating the left-lateral strike-slip motion of the NW-trending ZXf (Figure 9d). ZXf, an intra-crustal fault with a steep dip, has its NW segment dipping NE and its SE segment dipping SW, with the transition zone being a locked segment. Using the Burgers model [78], we studied the evolution of Coulomb stress induced by the 1936 M6¾ earthquake. This was performed by utilizing the PSGRN/PSCMP calculation program [79] and coseismic dislocation data [23,24]. The results show that the segment of ZXf between FLf1 and FLf2 are areas of increased Coulomb stress, with a maximum load of 1.0 MPa (Figure 9c), significantly higher than the typical seismic triggering threshold [80,81], indicating an enhanced risk of strong earthquakes in the segment of ZXf. The current stress field in the Lingshan seismic zone is characterized by a principal compressive stress that is oriented in a NWW–SEE direction, with a dip angle that is nearly horizontal. This favors

the left-lateral strike-slip motion of NW-trending faults and the right-lateral strike-slip of NE-trending faults [82,83]. The available evidence suggests that the locked part of ZXf, which was activated by the 1936 Lingshan M6¾ earthquake, reached a state close to rupture. Following an additional 22 years of the build-up of tectonic stress, the 1958 M5¾ Lingshan earthquake occurred.

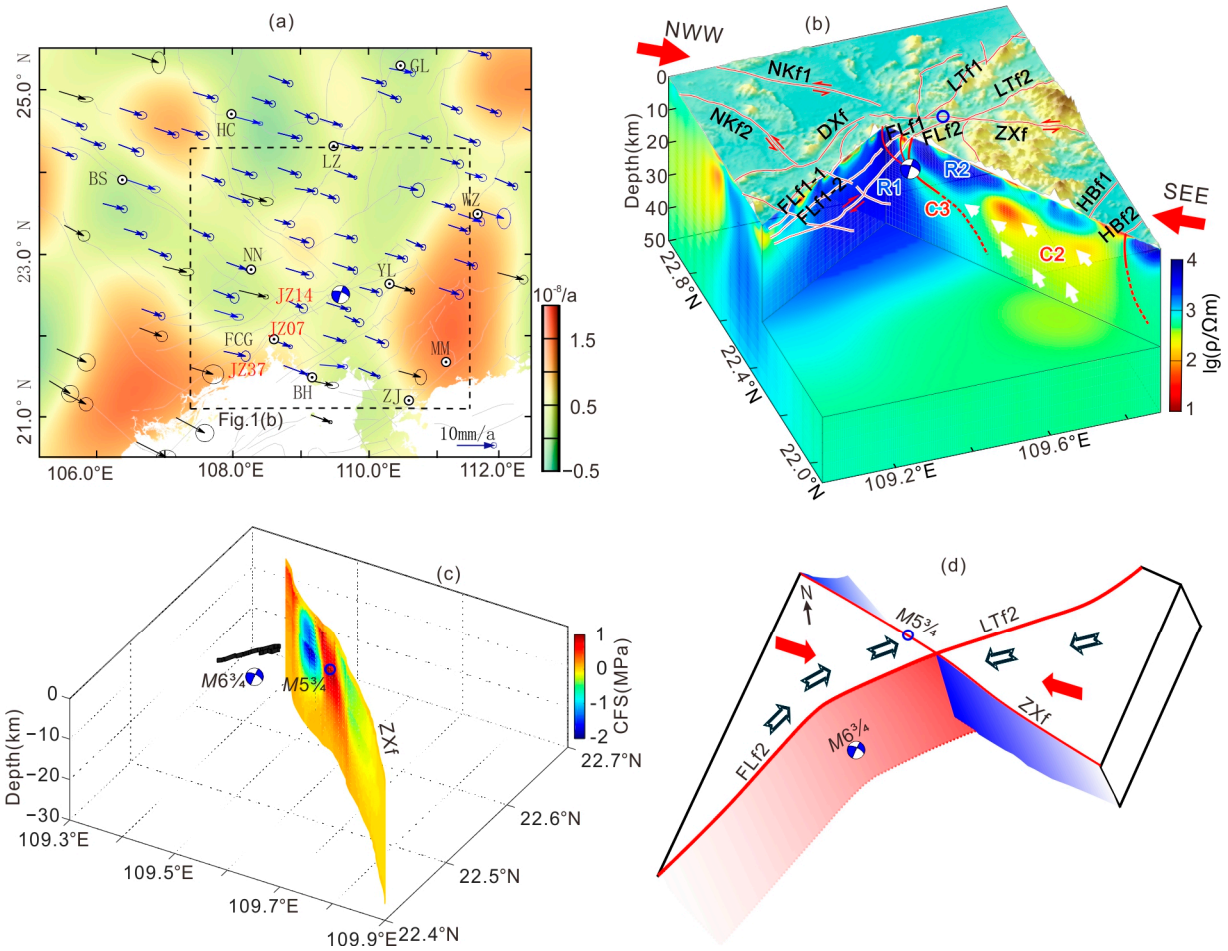

Figure 9. (**a**) GPS velocity field and plain strain rate distribution in the Lingshan earthquake region and its surrounding area. The small arrows indicate the GPS velocities. Error ellipses are 95% confidence interval. (**b**) 3D electrical structures in the Lingshan earthquake region. (**c**) The cumulated stress loading on the rupture plane of the 1958 M5¾ Lingshan earthquake associated with the 1936 M6¾ Lingshan earthquake (effective friction coefficient $\mu' = 0.4$). The black lines indicate coseismic surface rupture zone. (**d**) Cartoon diagram of conjugate seismic pattern of Lingshan earthquake. Red arrows indicate direction of tectonic stress field, and the black arrows indicate of coseismic displacement.

6. Conclusions

We have obtained broadband MT profile and surface array data that cover the Qinzhou fold belt in this research. Resistivity models for different profiles and conjugate tectonic zones were obtained using 3D electromagnetic inversion techniques. By combining geological, GPS, terrestrial heat flow, and static Coulomb stress triggering data, we conducted a comprehensive analysis of the deep extension of major faults, tectonic properties of different blocks, the deep seismogenic environment of the Lingshan seismic zone, and the conjugate rupture patterns, leading to the following insights:

The NE-trending faults within the Qinzhou fold belt and adjacent area are classified as trans-crustal faults and serve as electrical boundaries. The observed faults exhibit ductile

shear zones that extend into the mantle. The Fangcheng–Lingshan fault is buried within a high-resistivity body in the upper crust, with a southeastward-tilting electrical boundary at depth. It can be observed that the faults in the study area that trend towards the northeast are the main faults responsible for regional tectonic deformation and seismic activity. On the other hand, the faults that trend towards the northwest are smaller in scale and have a secondary role in regional tectonic deformation and seismic activity.

Various tectonic units in the Qinzhou fold belt and surrounding regions exhibit unique deep structural characteristics. The Shiwandashan and Dayaoshan Fault Depression exhibit layered resistivity structures, which are in line with the quasi-cratonic tectonic characteristics of localized damage on the southeastern edge of the Yangtze Block. The resistivity structure of the Qinzhou fold belt is a mix of high and low resistivities, corresponding to the characteristics of a composite orogenic belt that has undergone multiple phases of tectonic modification. There is a distinct pattern of high-resistivity layers in the upper crust and low-resistivity layers in the middle and lower crust between the Liuwandashan uplift and the Yunkai uplift. This indicates that there may be a connection to magmatic activities originating from the mantle in the Leiqiong area.

The Lingshan seismic zone displays an electrical structure characterized by "two low, one high". In the Lingshan fold belt, there is a prominent high-resistivity body surrounded by consistent low-resistivity bodies in the deeper section. There are low-resistivity anomalies present within the high-resistivity body, specifically along the eastern branch of the Fangcheng–Lingshan fault. Its surface projection covers the surface rupture zones of the 1936 M6¾ earthquake and the macro-seismic epicenter of the 1958 M5¾ earthquake. Compared to the low-resistivity bodies, the high-resistivity body displays harder rock properties and higher viscosity. Below 10 km in the Lingshan seismic zone, rock properties and rheology are distributed in an NE-trending band, controlling the deep structural framework of the seismic area. The NE-trending FLf is a larger-scale trans-crustal fault, while the NW-trending ZXf is a smaller-scale intra-crustal fault. The 1958 M5¾ earthquake was associated with the Zaixu Fault, and the macro-seismic epicenter is located precisely where the fault's dip changes. The conjugate rupture mode in the Lingshan seismic zone is likely determined by the differences in deep material properties, rheology, and fault development scale and depth.

The seismic source region of the Lingshan earthquake is mainly composed of intrusive rocks and clastic sedimentary rocks that are known for their rigid and unyielding nature. Under the coupling of regional tectonic stress and deep thermal dynamics, the strain is minimal, making it the main area of accumulated tectonic stress. When stress accumulation reaches the rock strength limit, the weaker FLf2 within the sub-high-resistivity strip experiences a dextral strike-slip rupture instability, resulting in the occurrence of an M6¾ earthquake in Lingshan. The coseismic deformation from this earthquake promoted sinistral strike-slip movement along the NW-trending ZXf in the conjugate fault system. The segment where the fault's dip changes becomes a locked section for stress accumulation and a Coulomb loading area for the 1936 M6¾ earthquake. The locked segment of ZXf continued to accumulate tectonic stress for 22 years before the occurrence of the 1958 M5¾ earthquake.

Supplementary Materials: The following supporting information can be downloaded at https://www.mdpi.com/article/10.3390/rs16193740/s1, Figure S1: 3D inversion mesh division; Figure S2: Fitting curves of apparent resistivity and phase for the 3D inversion; Figures S3 and S4: Model test for the detection depth; Figures S3 and S5: Model test for R1 and C3.

Author Contributions: Conceptualization, C.Y., B.Z. and Y.Z.; Resources, Y.Z. and X.S.; Data curation, Y.Z., X.S., S.L., L.L. and P.G.; Writing—original draft, C.Y., B.Z., Y.Z., S.L. and X.S.; Writing—review and editing, X.S. and S.L.; Project administration, Y.Z.; Funding acquisition, C.Y. All authors have read and agreed to the published version of the manuscript.

Funding: This work was supported by the National Natural Science Foundation of China (42374098, Yan Zhan), the Science for Earthquake Resilience program of the China Earthquake Administration

(XH24033B, Chunheng Yan), the Guangxi Scientific Research and Technology Development Plan Project (1377002, Bin Zhou; 14124004-4-8, Chunheng Yan), and the 2024 earthquake tracking and directional work tasks (2024020506, Chunheng Yan).

Data Availability Statement: Due to limitations of the project, data need to be kept confidential and cannot be shared.

Acknowledgments: The authors would like to thank Xiaobin Chen, Juntao Cai, and Zhongyin Liu for providing 3D inversion calculation MTP and toPeak software, Fuqiang Shi for assistance with Coulomb stress calculations, and the three anonymous reviewers for their valuable and constructive feedback. The 3D inversion was carried out on the 3D inversion calculation platform of MT data provided by the National Supercomputing Center, Institute of Geology, China Earthquake Administration. Some maps in this study were plotted using GMT [84].

Conflicts of Interest: The authors declare no conflicts of interest.

References

1. Parameswaran, R.M.; Thorbjarnardóttir, B.S.; Stefánsson, R.; Bjarnason, I.T. Seismicity on conjugate faults in Ölfus, South Iceland: Case study of the 1998 Hjalli-Ölfus earthquake. *J. Geophys. Res. Solid Earth* **2020**, *125*, e2019JB019203. [CrossRef]
2. Zhang, Y.; Chen, Y.T.; Xu, L.S.; Wei, X.; Jin, P.M.; Zhang, C. The 2014 M_W6.1 Ludian, Yunnan, earthquake: A complex conjugated ruptured earthquake. *Chin. J. Geophys.* **2015**, *58*, 153–162. [CrossRef]
3. Porreca, M.; Minelli, G.; Ercoli, M.; Brobia, A.; Mancinelli, P.; Cruciani, F.; Giorgetti, C.; Carboni, F.; Mirabella, F.; Cavinato, G.; et al. Seismic reflection profiles and subsurface geology of the area interested by the 2016–2017 earthquake sequence (Central Italy). *Tectonics* **2018**, *37*, 1116–1137. [CrossRef]
4. Kelly, P.G.; Sanderson, D.J.; Peacock, D.C.P. 1998. Linkage and evolution of conjugate strike-slip fault zones in limestones of Somerset and Northumbria. *J. Struct. Geol.* **2018**, *20*, 1477–1493. [CrossRef]
5. Taylor, M.; Yin, A.; Ryerson, F.J.; Kapp, P.; Ding, L. Conjugate strike-slip faulting along the Bangong-Nujiang suture zone accommodates coeval east-west extension and north-south shortening in the interior of the Tibetan Plateau. *Tectonics* **2003**, *22*, 1–21. [CrossRef]
6. Ma, J.; Ma, S.L.; Liu, L.Q.; Liu, T.C.; Wu, X.Q. Experimental study on alternate slip of intersecting faults and block movement. *Seismol. Geol.* **2000**, *22*, 65–73. [CrossRef]
7. Guo, T.T.; Xu, X.W.; Xing, H.L.; Yu, G.H. Nonlinear finite-element simulation of conjugate faults system and associated earthquake swarm. *Seismol. Geol.* **2015**, *37*, 598–612. [CrossRef]
8. Lozos, J.C. Dynamic rupture modeling of coseismic interactions on orthogonal strike-slip faults. *Geophy. Res. Lett.* **2022**, *49*, e2021GL097585. [CrossRef]
9. Lü, J.; Zheng, Y.; Ni, S.D.; Gao, J.H. Focal mechanisms and seismogenic structures of the M_s5.7 and M_s4.8 Jiujiang-Ruichang earthquakes of Nov.26, 2005. *Chin. J. Geophys.* **2008**, *51*, 158–164. [CrossRef]
10. Li, Y.Q.; Wang, D.; Xu, S.H.; Fang, L.H.; Cheng, Y.F.; Luo, G.; Yan, B.; Bogdan, E.; Mori, J. Thrust and Conjugate Strike-Slip Faults in the 17 June 2018 MJMA6.1 (M_w5.5) Osaka, Japan, Earthquake Sequence. *Seismol. Res. Lett.* **2019**, *90*, 2132–2141. [CrossRef]
11. Tadapansawut, T.; Yagi, Y.; Okuwaki, R.; Yamashita, S.; Shimizu, K. Complex rupture process on the conjugate fault system of the 2014 M_w6.2 Thailand earthquake. *Prog. Earth Planet. Sci.* **2022**, *9*, 26. [CrossRef]
12. Shinji, Y.; Yuji, Y.; Ryo, O.; Kousuke, S.; Ryoichiro, A.; Yukitoshi, F. Consecutive ruptures on a complex conjugate fault system during the 2018 Gulf of Alaska earthquake. *Sci. Rep.* **2021**, *11*, 5979. [CrossRef]
13. Barnhart, W.D.; Hayes, G.P.; Gold, R.D. The July 2019 Ridgecrest, California, Earthquake Sequence: Kinematics of Slip and Stressing in Cross-Fault Ruptures. *Geophys. Res. Lett.* **2019**, *46*, e2019GL084741. [CrossRef]
14. Goldberg, D.E.; Melgar, D.; Sahakian, V.J.; Thomas, A.M.; Xu, X.; Crowell, B.W.; Geng, J. Complex rupture of an immature fault zone: A simultaneous kinematic model of the 2019 Ridgecrest, CA earthquakes. *Geophys. Res. Lett.* **2020**, *47*, e2019GL086382. [CrossRef]
15. Wang, A.J.; Chen, Y.T. A method of determination of the internal friction characteristics within the Earth's crust through conjugate earthquakes. *Chin. J. Geophys.* **2021**, *64*, 3442–3451. [CrossRef]
16. Zhang, S.C. The great earthquake and the conjugate tectonic motion. *Seismol. Geol.* **1979**, *1*, 41–46.
17. Shu, L.S. An analysis of principal features of tectonic evolution in South China Block. *Geol. Bull. China* **2012**, *31*, 1035–1053. [CrossRef]
18. Wang, M.; Shen, Z.K. Present-day crustal deformation of Continental China derived from GPS and its tectonic implications. *J. Geophys. Res.* **2020**, *125*, e2019JB018774. [CrossRef]
19. Zhang, P.Z.; Deng, Q.D.; Zhang, Z.Q.; Li, H.B. Earthquake hazards and associated geodynamic processes in continental China. *Sci. China Earth Sci.* **2013**, *43*, 1607–1620.
20. Chen, G.D. *The Lingshan Earthquake on April 1, 1936*; The Geological Survey of Guangdong and Guangxi: Chengjiang, China, 1939; pp. 26–27. (In Chinese)
21. Mo, J.Y. *Earthquakes History of Guangxi*; Guangxi People's Publishing House: Nanning, China, 1990; pp. 60–62. (In Chinese)

22. Zhou, B.G.; Yang, X.P.; Du, L. Discussion on the Segmentation of Fangcheng-Lingshan Fault, Guangxi Province and Determination of Related Potential Seismic Sources. *Technol. Earthq. Disaster Prev.* **2008**, *3*, 8–19. [CrossRef]
23. Li, X.G.; Pan, L.L.; Li, B.S.; Nie, G.J.; Wu, J.B.; Lu, J.H.; Yan, X.M. Type and displacement characteristics of Lingshan M6¾ earthquake surface rupture zone in 1936, Guangxi. *Seismol. Geol.* **2017**, *39*, 904–916. [CrossRef]
24. Li, X.G.; Li, B.S.; Pan, L.L.; Nie, G.J.; Wu, J.B.; Lu, J.H.; Yan, X.M.; Li, Z.Y. A new finding of surface rupture zones associated with 1936 Lingshan M6¾ earthquake, Guangxi, China. *Seismol. Geol.* **2017**, *39*, 689–698. [CrossRef]
25. Zhou, B.; Yan, C.H.; Zhan, Y.; Sun, X.Y.; Li, S.; Wen, X.; Mo, Y.; Yuan, Y.D.; Yuan, Y.; Huang, M.L. Deep electrical structures of Qinzhou-Fangcheng Junction Zone in Guangxi and seismogenic environment of the 1936 Lingshan M6¾ earthquake. *Sci. Chin. Earth Sci.* **2024**, *67*, 584–603. [CrossRef]
26. Zhang, G.W.; Guo, A.L.; Wang, Y.J.; Li, S.Z.; Dong, Y.P.; Liu, S.F.; He, D.F.; Cheng, S.Y.; Lu, R.K.; Yao, A.P. Tectonics of South China continent and its implications. *Sci. Chin. Earth Sci.* **2013**, *56*, 1804–1828. [CrossRef]
27. Yan, J.Y.; Lü, Q.T.; Luo, F.; Chen, A.G.; Ye, G.F.; Zhang, Y.Q.; Zhang, K.; Zhao, J.H.; Zhang, C.; Liu, Z.D.; et al. Where is Qinzhou-Hangzhou juncture belt? Evidence from integrated geophysical exploration. *Chin. Geol.* **2019**, *46*, 690–703. [CrossRef]
28. Egbert, G.; Kelbert, A. Computational recipes for electromagnetic inverse problems. *Geophys. J. Int.* **2012**, *189*, 251–267. [CrossRef]
29. Kelbert, A.; Meqbel, N.; Egbert, G.D.; Tandon, K. ModEM: A modular system for inversion of electromagnetic geophysical data. *Comput. Geosci.* **2014**, *66*, 40–53. [CrossRef]
30. Yin, C.C.; Liu, Y.H.; Xiong, B. Status and prospect of 3D inversions in EM geophysics. *Sci. China Earth Sci.* **2020**, *63*, 452–455. [CrossRef]
31. Zhao, G.Z.; Unsworth, M.J.; Zhan, Y.; Wang, L.F.; Chen, X.B.; Jones, A.G.; Tang, J.; Xiao, Q.B.; Wang, J.J.; Cai, J.T.; et al. Crustal structure and rheology of the Longmenshan and Wenchuan Mw7.9 earthquake epicentral area from magnetotelluric data. *Geology* **2012**, *40*, 1139–1142. [CrossRef]
32. Zhan, Y.; Zhao, G.Z.; Unsworth, M.; Wang, L.F.; Chen, X.B.; Li, T.; Xiao, Q.B.; Wang, J.J.; Tang, J.; Cai, J.T.; et al. Deep structure beneath the southwestern section of the Longmenshan fault zone and seimogenetic context of the 4.20 Lushan M_S7.0 earthquake. *Chin. Sci. Bull.* **2013**, *58*, 3467–3474. [CrossRef]
33. Zhan, Y.; Liang, M.J.; Sun, X.Y.; Huang, F.P.; Zhao, L.Q.; Gong, Y.; Han, J.; Li, C.X.; Zhang, P.Z.; Zhang, H.P. Deep structure and seismogenic pattern of the 2021.5.22 Madoi (Qinghai) M_S7.4 earthquake. *Chin. J. Geophys.* **2021**, *64*, 2232–2252. [CrossRef]
34. Sun, X.Y.; Zhan, Y.; Unsworth, M.; Egbert, G.; Zhang, H.P.; Chen, X.B.; Zhao, G.Z.; Sun, J.B.; Zhao, L.Q.; Cui, T.F.; et al. 3-D Magnetotelluric Imaging of the Easternmost Kunlun Fault: Insights Into Strain Partitioning and the Seismotectonics of the Jiuzhaigou M_S7.0 Earthquake. *J. Geophys. Res. Solid Earth* **2020**, *125*, e2020JB019731. [CrossRef]
35. Ye, T.; Chen, X.L.; Huang, Q.H.; Cui, T.F. Three-dimensional electrical resistivity structure in focal area of the 2021 Yangbi Ms6.4 Earthquake and its implication for the seismogenic mechanism. *Chin. J. Geophys.* **2021**, *64*, 2267–2277. [CrossRef]
36. Unsworth, M.J.; Malin, P.E.; Egbert, G.D.; Booker, J.R. Internal structure of the San Andreas fault at Parkfield, California. *Geology* **1997**, *25*, 359–362. [CrossRef]
37. Becken, M.; Ritter, O.; Bedrosian, P.A.; Weckmann, U. Correlation between deep fluids, tremor and creep along the central San Andreas fault. *Nature* **2011**, *480*, 87–90. [CrossRef]
38. Xiao, Q.B.; Yu, G.; Zeng, J.L.; Oskin, M.E.; Shao, G.H. Structure and geometry of the Aksay restraining double bend along the Altyn Tagh Fault, northern Tibet, imaged using magnetotelluric method. *Geophys. Res. Lett.* **2017**, *44*, 4090–4097. [CrossRef]
39. Yang, B.; Egbert, G.D.; Zhang, H.Q.; Meqbel, N.; Hu, X.Y. Electrical resistivity imaging of continental United States from three-dimensional inversion of EarthScope USArray magnetotelluric data. *Earth Planet Sci. Lett.* **2021**, *576*, 117244. [CrossRef]
40. Corseri, R.; Planke, S.; Gelius, L.J.; Faleide, J.I.; Senger, K.; Abdelmalak, M.M. Magnetotelluric image of a hyper-extended and serpentinized rift system. *Earth Planet Sci. Lett.* **2023**, *602*, 11794. [CrossRef]
41. Regional Geological Survey Institute of Guangxi Zhuang Autonomous Region. *Guangxi Regional Geological Survey Area Summary and Service Product Development (China Regional Geology·Guangxi Chronicle) Project*; Regional Geological Survey Institute of Guangxi Zhuang Autonomous Region: Guilin, China, 2016. (In Chinese)
42. Qiu, L.; Yan, D.P.; Tang, S.L.; Wang, Q.; Yang, W.X.; Tang, X.; Wang, J. Mesozoic geology of southwestern China: Indosinian foreland overthrusting and subsequent deformation. *J. Asian Earth Sci.* **2016**, *122*, 91–105. [CrossRef]
43. Wu, J.Y. On the geological structural characteristics of Lingshan folding block zone. *Chin. J. Geol.* **1980**, *15*, 125–133.
44. Pan, G.T.; Xiao, Q.H.; Lu, S.N.; Den, J.F.; Feng, Y.M.; Zhang, Z.Y.; Wang, F.G.; Xing, G.F.; Hao, G.J.; Fang, Y.F. Subdivision of tectonic units in China. *Geol. China* **2009**, *36*, 1–28.
45. Huang, Q.X. The characteristics of some important basic geology in Guangxi. *Guangxi Geol.* **2000**, *13*, 3–12. [CrossRef]
46. Qin, X.F.; Li, J.; Li, R.S.; Zhou, F.S.; Hu, G.A.; Li, G.N.; Zhou, K.H.; Xie, L.F.; Pan, Y.W. *Formation and Evolution of the Bobai-Cenxi Orogenic Belt in the Northern Margin of the Yunkai Block*; China Land Press: Beijing, China, 2008. (In Chinese)
47. Zhang, Y.Q. Forel and thrust and nappe tectonics of shiwandashan. *Guangxi Geosci.* **1999**, *13*, 150–156.
48. Xu, H.L.; Yang, Y.N.; Shen, Y.; Ding, X. New Knowledges on Structural Features of Shiwandashan Basin, Guangxi. *Chin. J. Geol.* **2001**, *36*, 359–363. [CrossRef]
49. Liang, X.Q.; Li, X.H. Late Permian to Middle Triassic sedimentary records in Shiwandashan Basin: Implication for the Indosinian Yunkai Orogenic Belt, South China. *Sediment Geol.* **2005**, *177*, 297–320. [CrossRef]
50. Zhao, X.M.; Zhang, K.M.; Mo, W.R.; Wu, N.W.; Mao, X.W.; Ma, T.Q.; Huang, Y.Y.; Wang, H.R. *Description of Geotectonic Facies Map in Central and Southern China*; China University of Geosciences Press: Wuhan, China, 2015; pp. 1–119. (In Chinese)

51. Zhong, Z.Q.; You, Z.D.; Zhou, H.W.; Han, Y.Q. Composition, evolution and basic structural framework of basement of Yunkai uplift between Guangxi and Guangdong Provinces. *Reg. Geol. China* **1996**, *1*, 36–43.
52. Wang, Z.W.; Zhou, Y.Z.; Zhang, H.H.; Zhou, H.W. The basement evolution and mineralization of Yunkai Massif, South China. *Prog. Precam. Res.* **1998**, *21*, 45–53. [CrossRef]
53. Wang, X.D.; Xu, D.M.; Wang, L.; Zhou, D.; Hu, J.; Ke, X.Z. Reworking of Indosinian Tectono-Thermal Events in the Yunkai Massif: Gneissic Multi-Mineral U-Pb Geochronological Evidence. *Earth Sci.* **2020**, *45*, 1653–1675. [CrossRef]
54. Gamble, T.; Goubau, W.; Clarke, J. Magnetotellurics with a remote magnetic reference. *Geophysics* **1979**, *44*, 959–968. [CrossRef]
55. Egbert, G.; Booker, J. Robust estimation of geomagnetic transfer functions. *Geophys. J. R. Ustr. Soc.* **1986**, *87*, 173–194. [CrossRef]
56. Caldwell, T.G.; Bibby, H.M.; Brown, C. The magnetotelluric phase tensor. *Geophys. J. Int.* **2004**, *158*, 457–469. [CrossRef]
57. Bibby, H.M.; Caldwell, T.G.; Brown, C. Determinable and non-determinable parameters of galvanic distortion in magnetotellurics. *Geophys. J. Int.* **2005**, *163*, 915–930. [CrossRef]
58. Booker, J. The magnetotelluric phase tensor: A critical review. *Surv. Geophys.* **2014**, *35*, 7–40. [CrossRef]
59. Cai, J.T.; Chen, X.B.; Xu, X.W.; Tang, J.; Wang, L.F.; Guo, C.L.; Han, B.; Dong, Z.Y. Rupture mechanism and seismotectonics of the Ms6.5 Ludian earthquake inferred from three-dimensional magnetotelluric imaging. *Geophys. Res. Lett.* **2017**, *44*, 1275–1285. [CrossRef]
60. Heise, W.; Caldwell, T.; Bibby, H.; Bannister, S. Three-dimensional modelling of magnetotelluric data from the Rotokawa geothermal field, Taupo Volcanic Zone, New Zealand. *Geophys. J. Int.* **2008**, *173*, 740–750. [CrossRef]
61. Li, Y.H.; Gao, M.T.; Wu, Q.J. Crustal thickness map of the Chinese mainland from teleseismic receiver functions. *Tectonophysics* **2014**, *611*, 51–60. [CrossRef]
62. Ding, R.X.; Zou, H.P.; Lao, M.J.; Du, X.D.; Zhou, Y.Z.; Zeng, C.Y. Indosinian activity records of ductile shear zones in Southern segment of Qin-Hang combined belt: A case study of Fangcheng-Lingshan fault zone. *Earth Sci. Front.* **2015**, *22*, 79–85. [CrossRef]
63. Yan, C.H.; Li, S.; Zhou, B.; Zhan, Y.; Sun, X.Y.; Liu, X.H.; Su, S.; Liang, F.; Zhao, L.Q. Deep electrical structure of the hinterland of Yunkai magmatic arc in South China and the seismogenic environment of the 2019 Beiliu earthquake. *Front. Earth Sci.* **2023**, *11*, 1078796. [CrossRef]
64. He, G.Y.; Wu, C.L.; Pan, J.Y.; Yu, X.; Hu, A.P.; Jin, W.F.; Wu, L. New ideas on Western boundary fault of Qinzhou-Fangchenggang depression from hercynian to India-Chinese Epoch, Southeastern China. *Acta Geol. Sin.* **2007**, *81*, 1526–1530. [CrossRef]
65. Hu, L.S.; Xu, Y.J.; Du, Y.S.; Huang, H.W.; Xu, W.C.; Kuang, G.D. Geochemical characteristics and its geological significance of the late Paleozoic siliceous rocks in Qinfang Trough, southeastern Guangxi. *J. Palaeogeog.* **2014**, *16*, 77–87.
66. Cheng, Y.; Hu, X.; Han, B.; Li, Y.; Kong, Y.; Tang, J. Magnetotelluric evidence for lithospheric alteration beneath the Wuyi-Yunkai Orogen: Implications for thermal structure of South China. *Geochem. Geophys. Geosyst.* **2022**, *23*, e2022GC010456. [CrossRef]
67. Zhou, X.H.; Armstrong, R. Cenozoic volcanic rocks of eastern China-secular and geographic trends in chemistry and strontium isotopic composition. *Earth Planet Sci. Lett.* **1982**, *58*, 301–329. [CrossRef]
68. Flower, M.F.J.; Zhang, M.; Chen, C.Y.; Tu, K.; Xie, G.H. Magmatism in the South China Basin 2. Post-spreading Quaternary basalts from Hainan Island, south China. *Chem. Geol.* **1992**, *97*, 65–87. [CrossRef]
69. Zou, H.; Fan, Q.C. U-Th isotopes in Hainan basalts: Implications for sub-asthenospheric origin of EM2 mantle endmember and the dynamics of melting beneath Hainan Island. *Lithos* **2010**, *116*, 145–152. [CrossRef]
70. Huang, H.B.; Tosi, N.; Chang, S.J.; Xia, S.H.; Qiu, X.L. Receiver function imaging of the mantle transition zone beneath the South China Block. *Geochem. Geophys. Geosyst.* **2015**, *16*, 3666–3678. [CrossRef]
71. Xia, S.H.; Zhao, D.P.; Sun, J.L.; Huang, H.B. Teleseismic imaging of the mantle beneath southernmost China: New insights into the Hainan plume. *Gondwana Res.* **2016**, *36*, 46–56. [CrossRef]
72. Wei, S.S.; Chen, Y.J. Seismic evidence of the Hainan mantle plume by receiver function analysis in southern China. *Geophys. Res. Lett.* **2016**, *43*, 8978–8985. [CrossRef]
73. Yan, Q.S.; Shi, X.F.; Metcalfe, L.; Liu, S.F.; Xu, T.Y.; Kornkanitnan, N.; Sirichaiseth, T.; Yuan, L.; Zhang, Y.; Zhang, H. Hainan mantle plume produced late Cenozoic basaltic rocks in Thailand, Southeast Asia. *Sci. Rep.* **2018**, *8*, 2640. [CrossRef]
74. Yuan, Y.S.; Ma, Y.S.; Hu, S.P.; Guo, D.L.; Fu, X.Y. Present-day geothermal characteristics in South China. *Chin. J. Geophys.* **2006**, *49*, 1118–1126. [CrossRef]
75. Sun, M.X.; Zhang, Q.Z.; Liu, D.M.; Sun, X.T.; Lin, S.; Wu, X.K.; Liang, G.K.; Li, Y.K.; Guan, Y.W.; Li, Y.F. Genesis and occurrence models of hot-dry geothermal resources in Guangxi. *Bull. Geol. Sci. Technol.* **2022**, *41*, 330–340. [CrossRef]
76. Zhang, Q.W.; Zhang, P.Z.; Wang, C.; Michael, A.E. Interaction of active faults and its effect on earthquake triggering and delaying. *Acta Geosci. Sin.* **2004**, *25*, 483–488. [CrossRef]
77. Zhou, S.Y. Seismicity Simulation in Western Sichuan of China based on the Fault Interactions and Its Implication on the Estimation of the Regional Earthquake Risk. *Chin. J. Geophys.* **2008**, *51*, 165–174. [CrossRef]
78. Shao, Z.G.; Fu, R.S.; Xue, T.X.; Huang, J.H. Simulating postseismic viscoelastic deformation based on Burgers model. *J. Geod. Geodyn.* **2007**, *27*, 31–37. [CrossRef]
79. Wang, R.; Lorenzo-Martin, F.; Roth, F. PSGRN/PSCMP—A new code for calculating co- and post-seismic deformation, geoid and gravity changes based on the viscoelastic-gravitational dislocation theory. *Comput. Geosci.* **2006**, *32*, 527–541. [CrossRef]
80. King, G.C.P.; Stein, R.S.; Lin, J. Static stress changes and the triggering of earthquakes. *Bull. Seismol. Soc. Am.* **1994**, *84*, 935–953. [CrossRef]

81. Shi, F.Q.; Xiong, X.; Wang, P.T.; Su, L.N.; Shan, B.; Zhu, L.; Shao, Z.G. Stress interaction between the two M > 6 earthquake since 2016 and its implication on the seismic hazard along the Qilian-Haiyuan fault zone. *Chin. J. Geophys.* **2023**, *66*, 3230–3241. [CrossRef]
82. Jiang, W.; Lin, J.; Zhao, Y. Focal mechanism of small earthquakes and characteristics of the tectonic stress field in South China. *Earth Res. China* **1992**, *8*, 36–42.
83. Wan, Y. Contemporary tectonic stress field in China. *Earthq. Sci.* **2010**, *23*, 377–386. [CrossRef]
84. Wessel, P.; Smith, W.H.F.; Scharroo, R.; Luis, J.; Wobbe, F. Generic mapping tools: Improved version released. *Eos Trans. Am. Geophys. Union* **2013**, *94*, 409–410. [CrossRef]